Passivation of Grain Boundaries by Selenium in Alloyed CdTe Solar Cells

Thomas Fiducia*, Ashley Howkins, Ali Abbas, Budhika Mendis, Amit Munshi, Kurt Barth, Walajabad Sampath, and John Walls

Dr. Thomas Fiducia, Dr. Ali Abbas, Prof. John Walls
Loughborough University, Leicestershire, LE11 3TU, UK.
E-mail: T.A.M.Fiducia@lboro.ac.uk

Dr. Ashley Howkins
Brunel University London, Uxbridge, UB8 3PH, UK.

Dr. Budhika Mendis
Durham University, Durham, DH1 3LE, UK

Dr. Amit Munshi, Prof. Kurt Barth, Prof. Walajabad Sampath
Colorado State University, Fort Collins, Colorado, USA.

Keywords: cadmium telluride, grain boundaries, selenium, TEM, cathodoluminescence

Cadmium telluride (CdTe) solar cells have achieved efficiencies of over 22%, despite having absorber layer grain sizes less than 10 μm and hence a very high density of grain boundaries. Recent research has shown that this is possible because of partial passivation of grain boundaries during the widely used cadmium chloride treatment, and passivation of grain interior defects by selenium alloying of the CdTe. Here, state-of-the art TEM-based cathodoluminescence imaging is used to show that, in addition to grain interiors, selenium also passivates grain boundaries in alloyed $Cd(Se_x,Te_{1-x})$. We find that up to $x = 0.2$, higher selenium concentrations at grain boundaries results in improved passivation. This further explains the superior performance of selenium graded CdTe devices and provides potential new routes for further efficiency improvement and solar electricity cost reduction.

1. Introduction

In the last decade, the efficiency of cadmium telluride (CdTe) solar cells has risen from 16.7% to the current record of 22.1% [1]–[3]. This is significantly higher than for the best polycrystalline gallium arsenide cells at 18.4%, and near the record for multi-crystalline silicon cells at 22.3%, despite the fact that CdTe grains are more than 1,000 times smaller than silicon grains by diameter [3]–[5] (CIGS devices, which also have small grain sizes, have reached efficiencies of 23.35% [3]). Three discoveries in CdTe solar cell research have helped to explain the high CdTe device performance, despite its fast-grown, high defect density absorber material, all of which relate to the introduction of either chlorine or selenium into the CdTe.

Firstly it was found that during the cadmium chloride ($CdCl_2$) heat treatment, which is used universally to produce high efficiency CdTe cells, chlorine segregates to grain boundaries in the CdTe and partially passivates them [6]–[10]. Barnard et al then showed that in addition to grain boundaries, the treatment also increases carrier lifetimes in the interiors of CdTe grains, and at the front interface of the absorber [11]–[13]. Finally, in 2019 our group used SEM-based cathodoluminescence (SEM-CL) to show that selenium, which was initially alloyed with CdTe at the front of the absorber layer to decrease its bandgap, also has a passivation effect on grain interiors in both treated and untreated Cd(Se,Te) [14], [15]. This helped to explain the superior optoelectronic properties of polycrystalline Cd(Se,Te), which can have higher carrier lifetimes than even single-crystal CdTe (750 ns, vs 670 ns for the best single crystal CdTe [16], [17]). However, while the SEM-CL data clearly showed the positive effects of selenium in the interiors of Cd(Se,Te) grains, it did not show whether it affects recombination at grain boundaries. Low contrast defects such as passivated grain boundaries are hard to resolve in SEM-CL, since it has an electron beam-sample interaction volume of more than 250 nm (diameter) in CdTe, even at high resolution beam settings (7.5 keV beam energy, with 75% of carriers generated within this volume [18]).

The effects of selenium on the electronic properties of CdTe grain boundaries has been modelled in several recent papers using density functional theory (DFT). Calculations by Guo et al [19], [20] suggested that co-doping of selenium and chlorine at a CdTe dislocation core reduced the density of mid-gap states associated with the defect. Modelling by Wei et al [21] suggested that selenium segregates to Te-core CdTe grain boundaries, substitutes with tellurium, and reduces the depth and density of mid-gap states. And most recently, Shah et al [22] modelled chlorine and selenium at a CdTe grain boundary and concluded that together the elements reduced the density of harmful mid-gap defect states.

Despite this modelling work, real-world evidence of CdTe grain boundary passivation with selenium is limited. In 2019, Zheng et al [23] performed time-resolved PL mapping on a bilayer Cd(Se,Te)/CdTe device and found that carrier lifetimes were more homogeneous (and higher) in the Cd(Se,Te) layer than the CdTe, suggesting lower levels of grain boundary recombination in the Cd(Se,Te). And recently, in 2021, Amarasinghe et al [24] performed SEM-CL mapping on test Cd(Se,Te) and CdTe double heterostructures that had alumina either side of the absorber, and found that the drop in luminescence intensity at Cd(Se,Te) grain boundaries was lower than at CdTe grain boundaries.

Here, we assess the electronic effects of selenium on Cd(Se,Te) grain boundaries using high resolution CL imaging in a scanning transmission electron microscope (STEM-CL) [25]. Whereas high resolution STEM-CL imaging of a solar cell has previously not been achieved because of problems with low signal, we use cryogenic cooling of the TEM foil and xenon ion milling of the sample to boost the CL signal and overcome this issue [26]. Using STEM-CL allows us to directly correlate the CL maps to TEM micrographs of the absorber layer microstructure and high-resolution STEM-EDX maps of elemental composition, which is a key benefit of the TEM-based technique. The results provide direct evidence that selenium has a passivation effect on grain boundaries in alloyed Cd(Se,Te) material – on top of what can be achieved with chlorine alone. This further explains how polycrystalline selenium-graded CdTe devices can compete on efficiency with large-grained, slow-grown, and more expensive competitors like silicon [27].

To perform the investigation, two bilayer Cd(Se,Te)/CdTe solar cells were fabricated at Colorado State University as described in the methods section. One of the samples was left as-deposited while the other received a cadmium chloride ($CdCl_2$) heat treatment. Cross-sectional TEM foils (~125 nm thick) were then ion milled and ‘lifted out’ from the samples. Crucially, in order to maximise the luminescence signal from the foils, the ion milling was performed using a xenon focused ion beam (FIB), as opposed to the traditional gallium FIB. Because of the higher atomic mass of xenon there is less implantation of ions into the sample during milling. This reduces the number of harmful point defects that are introduced to the sample, reducing the number of non-radiative recombination channels available to carriers and therefore increasing the luminescence signal. In addition, because xenon is inert, the defects that are formed are less likely to be harmful than those created by gallium implantation. To confirm the superior electronic properties of xenon milled CdTe compared to gallium milled material, we ion milled two bevelled trenches adjacent to each other in a CdTe film, one with a xenon beam and one with a gallium beam and compared the SEM-CL signal from the two bevels. The results are shown in Figure S1 in the supplementary information.It can be seen that the CL signal from the Ga milled bevel is significantly lower than the signal from the Xe milled bevel. Moreover, the level of CL signal from the xenon milled bevel is similar to that from the unprepared CdTe surface either side of the trench, showing that xenon ion milling introduces minimal defects compared to a normal, unprepared CdTe surface.

In addition to using a Xe milled lamella, another way to improve the luminescence signal from a sample is to cryogenically cool it down as this increases the efficiency of radiative recombination. As such, during the STEM-CL measurements, liquid nitrogen was used to cool the lamellae to approximately -170 °C. We found cooling to be particularly important, and without it, the CL signal was very low even with a xenon ion milled sample.

2. Results

2.1. As-deposited device

A cross-sectional TEM micrograph of the as-deposited Cd(Se,Te)/CdTe bilayer device is shown in **Figure 1a**. Generally, small columnar grains are seen in the Cd(Se,Te) layer, and larger grains in the CdTe. However, there are some instances where the CdTe has grown epitaxially on the Cd(Se,Te)material and formed continuous grains that span the two layers (see dashed lines in the figure). The distribution of selenium within the cross-section is shown in the STEM-EDX map in Figure 1b. It shows that selenium (~10 at%) is contained within the Cd(Se,Te) layer, with no detectable diffusion into the CdTe during deposition [28]. This is mirrored by the tellurium EDX signal distribution in Figure 1c, which shows higher tellurium signal in the CdTe and lower signal in the Cd(Se,Te) as expected.

The cathodoluminescence signal distribution over the bilayer is shown in Figure 1d. In the CdTe region at the top of the absorber, the CL signal is low, with counts in the grain interior (2.65 x10^6) barely reaching higher than the background level, taken from the platinum region of the lamella (2.39 x10^6). This is expected because it is known that as-deposited CdTe material has a low luminescence efficiency, particularly compared to $CdCl_2$ treated CdTe [11], [29], [30]. However, there is sufficient signal to distinguish dark contrast at the CdTe grain boundaries, which is due to increased non-radiative carrier recombination at grain boundary defects (dangling bonds, wrong bonds, etc) compared to the grain bulk.

In the Cd(Se,Te) layer, the cathodoluminescence signal is significantly brighter than in the CdTe, despite the smaller Cd(Se,Te)grains (background-subtracted counts reach ~1.8 x10^6 in the Cd(Se,Te), compared to a maximum of ~0.26 x10^6 in the CdTe). This is consistent with our recent SEM-based CL results which show that selenium alloying significantly increases luminescence efficiency within the grain bulk of both treated and untreated Cd(Se,Te) material [14], [15]. Values of grain boundary contrast in the Cd(Se,Te) and CdTe are similar at ~50%, however the width of the grain boundary contrast in the Cd(Se,Te) is only ~250-300 nm, compared to an average contrast width of ~500 nm in the CdTe (shown to scale on the image for comparison).

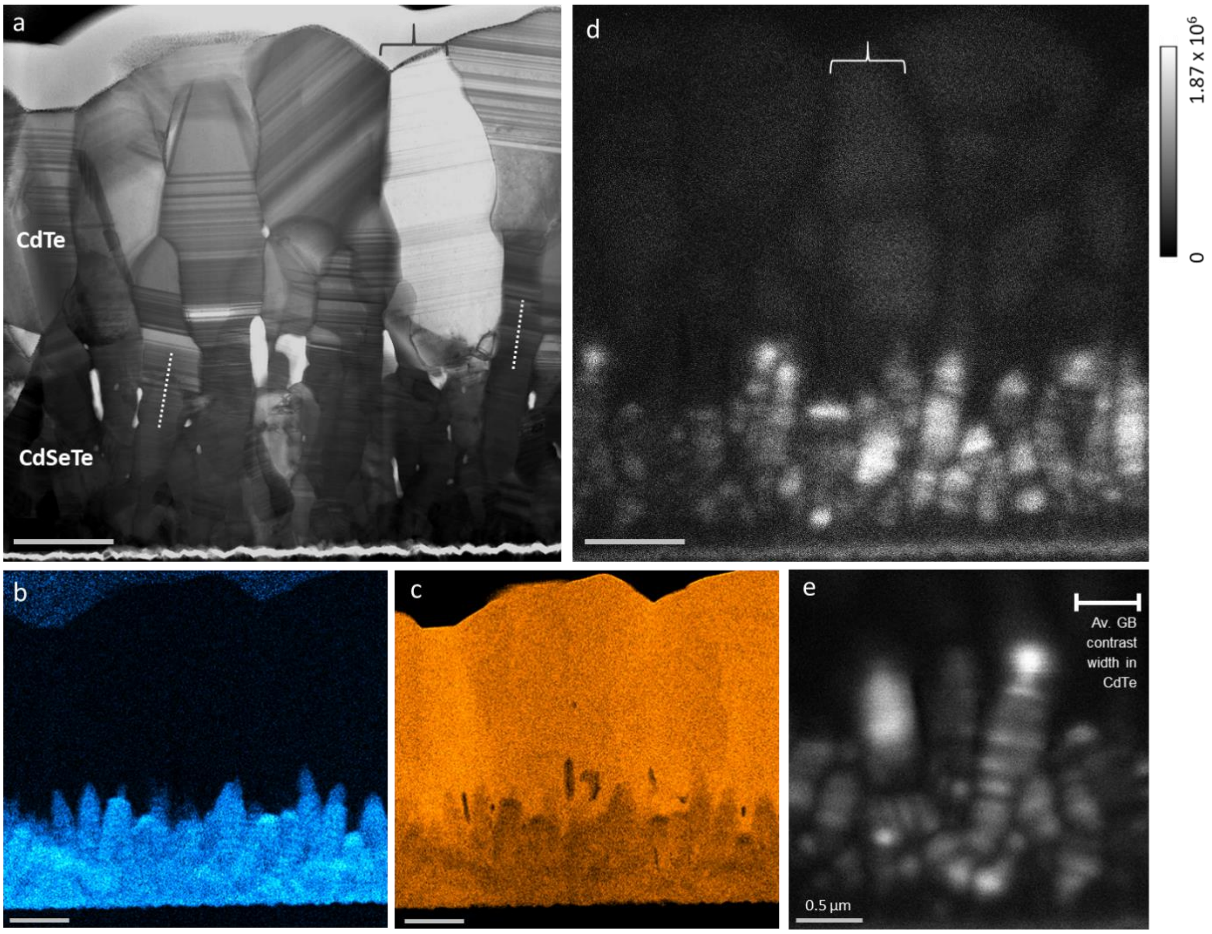

Figure 1. **a** Cross-sectional TEM micrograph of the as-deposited Cd(Se,Te)/CdTe device, with dashed lines showing where CdTe has grown epitaxially on Cd(Se,Te) grains. **b** EDX map of the selenium signal distribution over the cross-section, with brighter blue showing higher signal. **c** EDX map of the tellurium signal distribution over the cross section, with brighter orange showing higher signal. **d** Low-temperature STEM-based cathodoluminescence (CL) map (-169.3 °C) of the luminescence signal over the cross-section, with the field of view shifted slightly from that in **a** (the brackets in **a** and **d** show the same grain). The intensity scale bar shows background-subtracted counts. **e** Higher magnification image of the CL intensity variations over a region in the Cd(Se,Te) layer. The measure in the top right of the image shows the average contrast width of the CdTe grain boundaries at this magnification. All scale bars are 1 µm except in **e.**

As well as dark contrast between grains, there are also signal variations within grains in the Cd(Se,Te) layer. These are shown more clearly in the higher magnification image in Figure 1e, where it can be seen that the signal variations are bands of brighter and darker contrast within the Cd(Se,Te) grains. Comparison with the TEM micrographs shows that these bands run parallel to the (111) twinning plane of the grains, indicating that the in-grain signal variations are caused by twinning of the Cd(Se,Te). This could be due to increased carrier recombination at regions of highly faulted or hexagonal phase material, or to variations in the defect density at different crystal surfaces (111, 100, etc) which are exposed during the milling of the TEM lamella surfaces and which are affected by twinning [15].

2.2. Cadmium chloride treated device

A TEM micrograph of the cadmium chloride treated Cd(Se,Te)/CdTe device is shown in **Figure 2a**. In contrast to the untreated device, which has a bilayer structure, there are no distinct Cd(Se,Te) and CdTe layers in the treated absorber and grain sizes are generally larger. This shows that there

has been recrystallisation of the absorber layer during the cadmium chloride heat treatment. An EDX map of the selenium signal distribution in the cross-section is shown in Figure 2b, and in Figure 2c this map has been superimposed on top of the TEM micrograph. Compared to the untreated device, the maps show a more gradual decrease in selenium signal from the front to the back of the film. This indicates that during the $CdCl_2$ treatment, selenium diffuses from the Cd(Se,Te) layer into the CdTe [31]. In the interdiffused region between the top and bottom of the film, higher selenium signal is seen at grain boundaries compared to the adjacent bulk (e.g. circled grain boundary in Figure 2b), indicating that grain boundaries provide a pathway for preferential diffusion of selenium into the CdTe layer [28]. The EDX map for chlorine is shown in Figure 2e and indicates segregation along the grain boundaries, consistent with previous reports [7], [8], [28]. In Figure 2e there appears to be less chlorine segregation at some grain boundaries in the CdTe region at the top of the film. This is an experimental artefact caused by the large inclination of these grain boundaries within the TEM foil (see Figure 2a), resulting in a large GB projected width and less sensitivity of the measured EDX signal to chlorine segregation. CdTe grain boundaries that are close to being 'end-on' (e.g. the arrowed grain boundary in Figure 2e) show the expected chlorine signal enhancement. Furthermore, EDX measurements on different regions of the sample show that chlorine is present along grain boundaries throughout the film thickness (see Figure S4).

A STEM-CL map acquired on the device cross-section is shown in Figure 2d. Unlike in the untreated device, the CL signal in the grain interior of the CdTe is significantly higher than the background counts, measured at the platinum layer (2.34×10^6 background counts vs 3.05×10^6 counts in the CdTe). Although counts between different samples are not directly comparable, this suggests that grain interior luminescence in the treated CdTe is higher than in the untreated device. Higher grain interior signal enables clear grain boundary contrast to

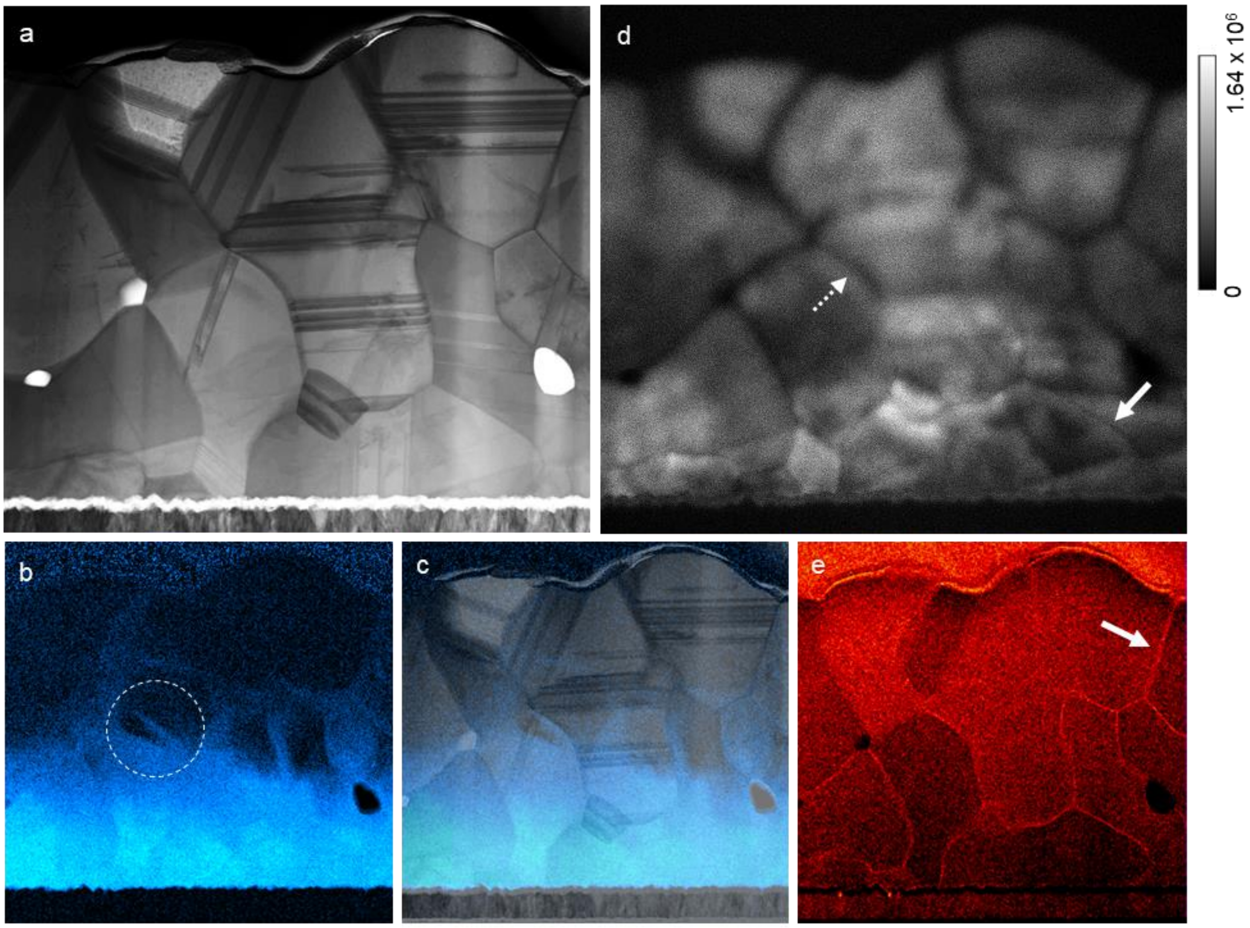

Figure 2. **a** Cross-sectional bright field TEM micrograph of the cadmium chloride treated Cd(Se,Te)/CdTe device, with a field of view of 6.8 µm x 6.1 µm (same for all the panels in the figure). **b** EDX map of the selenium distribution in the cross section (brighter blue shows higher selenium signal intensity). **c** Map of the selenium signal distribution in **b**, superimposed on top of the micrograph in **a**. **d** Low-temperature STEM-based cathodoluminescence (CL) map (-170.6 °C) of the panchromatic CL intensity over the cross-section, with arrows highlighting the thinner grain boundary contrast in the interdiffused region (dashed arrow) and Cd(Se,Te) (solid arrow) versus the CdTe. Intensity scale bar shows background-subtracted counts, with the background taken at the platinum region above the CdTe. **e** EDX map of the chlorine signal intensity over the cross-section. The arrow shows an 'edge on' grain boundary in the CdTe.

be seen in the treated sample. However, there is significant variation in the amount of contrast at grain boundaries depending on their depth through the absorber. In the CdTe region towards the top of the film there are thick, dark bands of grain boundary contrast. At the bottom of the film, in the Cd(Se,Te) material, there are only thin, faint lines of contrast (see the solid arrowed grain boundary in the figure). For instance, the width of GB contrast in three of the CdTe boundaries in the image are all between 500-600 nm, with a grain boundary contrast of between 63-78%. This means that the signal at the trough of the V-shaped CL profile is 63-78% lower than the averaged signal on both sides of the boundary (see the CL profile in Figure S2 in the Supplementary Information for example). This compares to the arrowed boundary in the Cd(Se,Te), where the GB contrast is only 29%, with a width of 100 nm (see supplementary Figure S2). This reduction in grain boundary contrast and width shows that there is significantly lower carrier recombination in the Cd(Se,Te) grain boundaries compared to CdTe. Since the bilayer has been $CdCl_2$ treated, this is 'extra' GB passivation – on top of what can be achieved purely with chlorine at the grain boundaries. In addition, the data shows that the level of grain boundary passivation is dependent on the amount of selenium at each specific boundary. For instance, a boundary with an intermediate concentration of selenium around it has been circled in the selenium map in Figure 2b. It can be seen in the CL map (dashed arrow) that the contrast at this boundary is also intermediate, i.e lower than that at pure CdTe boundaries, but higher than at boundaries in the Cd(Se,Te). This indicates that for the selenium concentration ranges present in this cell (i.e. 0 – 10 at%), the more selenium present at and around a boundary, the greater the passivation of the boundary.

It is possible to extract the recombination velocity of individual grain boundaries from CL images, as has previously been demonstrated for SEM-CL [32]. The CL contrast $\Delta I(x)$ at a distance x from the grain boundary is given by [32]:

$$log[\Delta I(x)] = log\left(\frac{S_{red}}{S_{red}+1}\right) - \frac{x}{L} \qquad (1)$$

where L is the minority carrier diffusion length and S_{red} is the reduced recombination velocity. S_{red} is related to the grain boundary recombination velocity (S) by $S_{red} = S\tau/L$, where τ is the carrier lifetime. The CL contrast is defined as $\Delta I(x) = 1 - [I(x)/I_o]$, where I(x) is the CL intensity at distance 'x' from the grain boundary and I_o is the plateau CL intensity at the grain interior [32]. The CL intensities were background subtracted prior to analysis (the background was defined using the platinum layer). By plotting $\log[\Delta I(x)]$ as a function of x the diffusion length L and reduced recombination velocity S_{red} can be extracted.

In this model it is assumed that free surface recombination can be ignored. While this can be approximately satisfied in SEM by increasing the energy of the incident beam, it is not possible to ignore surface recombination in TEM-CL. Despite this, a recent TEM-CL study by Yoon et al [33] has shown that Equation (1) can still be applied, provided the lifetime τ is replaced by an effective lifetime τ_{eff} that is lower than the bulk value. τ_{eff} is determined by surface recombination and is a function of the TEM specimen thickness. The effective diffusion length is then $L_{eff} = \sqrt{(D\tau_{eff})}$, where D is the carrier diffusion coefficient.

Applying Equation (1) to our TEM-CL data would yield effective values for the diffusion length and reduced recombination velocity. Since these values depend on the specimen thickness they are not very useful on their own. However, it does enable us to compare different grain boundaries provided the data are all extracted from the same specimen.

Figure 3a shows the TEM-CL map (same as Figure 2d) with the analysed grain boundaries indicated in numerical order. Three CdTe and three Cd(Se,Te) grain boundaries were found to be suitable for quantitative analysis. Figure 3b shows an example CL intensity profile across a grain boundary and Figure 3c its linearisation according to Equation (1). The linearisation plots for the grain boundaries all had regression coefficients larger than 0.95, apart from grain boundary 5 which had a lower regression coefficient of 0.87. When selecting Cd(Se,Te) grain boundary profiles, care was taken to ensure the selenium concentration was uniform over the region of interest; this was done by comparing with the EDX map for selenium (Figure 2b).

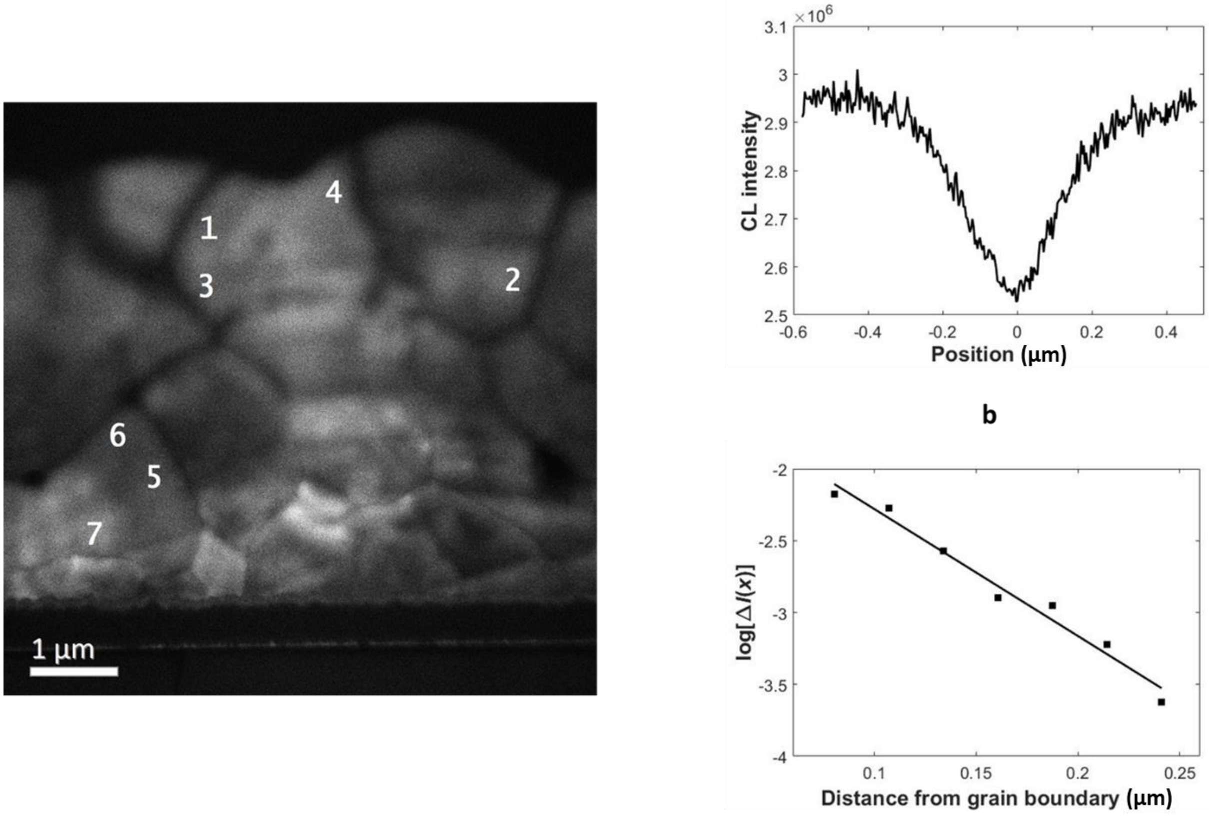

b

a

c

Figure 3. **a** TEM-CL image of the treated bilayer device with the analysed grain boundaries indicated in numerical order. **b** shows the CL intensity profile across one of the grain boundaries (grain boundary 1) and **c** is its linearisation according to Equation (1).

The effective diffusion length and recombination velocity values for CdTe and Cd(Se,Te) grain boundaries are listed in Tables 1 and 2 respectively. The average value for the effective diffusion length in Cd(Se,Te) is slightly smaller than CdTe, i.e. 0.11 μm vs 0.14 μm. Since $L_{\mathrm{eff}} = \sqrt{(D\tau_{\mathrm{eff}})}$ this could be due to differences in τ_{eff} as well as the diffusion coefficient D between CdTe and CST regions. The TEM-CL measurements are strongly influenced by surface recombination and are performed at liquid nitrogen temperature. Therefore, the effective diffusion lengths reported here must not be confused with the bulk diffusion lengths that are relevant for room temperature photovoltaic device operation. Furthermore, Monte-Carlo simulations have shown that the steady-state carrier distribution volume within a 100 nm thick, CdTe TEM foil has similar dimensions to the effective diffusion length [26], i.e. the carrier concentration drops to 50% of its maximum value within a distance of ~0.1 μm. Scattering of the electron beam within the TEM specimen should therefore have some influence on extracted values for L_{eff}. Apart from grain boundary 3 in

Table 1 the reduced recombination velocity of CdTe grain boundaries is more than an order or magnitude larger than the average for Cd(Se,Te) boundaries, i.e. $S_{red} = 2.63$. The large variation in the extracted values supports the conclusion that significant grain boundary passivation occurs in CST over and above CdTe.

Table 1. Effective diffusion length and reduced recombination velocity values for CdTe grain boundaries (numbers 1 to 3 in
Figure *3*a).

Grain boundary	Effective diffusion length L_{eff} (μm)	Reduced recombination velocity S_{red}
1	0.13 ± 0.01	34.84 ± 127.35
2	0.16 ± 0.01	41.00 ± 94.71
3	0.13 ± 0.01	4.70 ± 2.25

Table 2. Effective diffusion length and reduced recombination velocity values for Cd(Se,Te) grain boundaries (numbers 4 to 6 in
Figure *3*a).

Grain boundary	Effective diffusion length L_{eff} (μm)	Reduced recombination velocity S_{red}
4	0.10 ± 0.01	5.64 ± 0.02
5	0.15 ± 0.03	1.42 ± 0.19
6	0.07 ± 0.01	0.83 ± 0.14

The recombination velocity is a measure of the carrier 'lifetime' at a grain boundary; the larger its value the stronger the recombination and therefore more harmful to device performance. Many of the grain boundaries deep within the Cd(Se,Te) layer show too little contrast to carry out a meaningful quantitative analysis. We have nevertheless been able to analyse grain boundaries in the regions with intermediate selenium concentration, where the contrast is slightly higher. The results indicate that grain boundary recombination in the intermediate Cd(Se,Te) layer can be an order of magnitude smaller than some CdTe grain boundaries. The true value would be even smaller for Cd(Se,Te) grain boundaries with high selenium concentration. It should be noted that grain boundary projected width does not have a large effect on grain boundary contrast in the CdTe, since the CL resolution is governed by the effective carrier diffusion length, which is ~100 nm even for TEM-CL (see Tables 1 and 2).

One feature of the STEM-CL map in Figure 2d is that the bulk Cd(Se,Te) material does not show brighter CL signal than the CdTe bulk, as would be expected from our previous SEM-CL measurements. We believe that this is because of the proximity of the free surfaces of the TEM lamella, which are separated by less than 150 nm. In this situation, any increase in the carrier diffusion length caused by selenium alloying only makes it more likely that the generated carriers will diffuse to the lamella surfaces and be quenched. This highlights one disadvantage of STEM-CL, which is the proximity of the ion milled lamella surfaces, and suggests that lamella surface passivation, perhaps with alumina, could be a good way to improve STEM-CL imaging further [34]. Despite this, our other STEM-CL measurements of bilayer films have shown the expected brighter luminescence in the Cd(Se,Te). One of these is shown in Figure S3 in the Supplementary information. It can be seen that as well as having brighter Cd(Se,Te) compared to CdTe, the width of the grain boundary contrast is thinner in the Cd(Se,Te) than the CdTe, as we have seen in Figure 2. In addition, another example of a measurement showing brighter Cd(Se,Te) is shown in Figure 4a in the next section. It could be argued that the thin grain boundary contrast observed for Cd(Se,Te) is an artefact of electron beam injection, since the doping concentration is likely to be different between the CdTe and Cd(Se,Te) layers. The fact that these thicker specimens with brighter CL signal for the Cd(Se,Te) layer also show thin grain boundary contrast effectively rules out electron beam injection artefacts. The thicker specimens have higher injection levels due to the incident electron beam losing more of its energy and due to the diminished role of free surface recombination. Despite this there is still a clear difference between CdTe and Cd(Se,Te) grain boundary contrast, indicating that it is a real effect.

2.3. Hyperspectral STEM-CL

A panchromatic map of the CL signal intensity over a treated bilayer cross-section, from the same device as that in Figure 2 but taken from a different area of the film, is shown in **Figure 4a**. Lower CL signal is seen at the top of the film in the CdTe, and higher signal in the Cd(Se,Te), and there is a thick region of grain boundary contrast in the CdTe. A low-temperature hyperspectral CL map, where a full luminescence spectrum is collected in each step of the electron beam raster, was performed on this sample. Figure 4b shows a comparison of the average CL spectrum in the CdTe part of the sample (black curve) with the average spectrum in the Cd(Se,Te) part of the sample (blue curve). The CdTe spectrum shows a sharp excitonic peak at 1.59 eV and a broader peak at 1.43 eV, which we attribute to donor-acceptor-pair (DAP) emission [35]. The Cd(Se,Te) spectrum has similar excitonic and DAP peaks, but their peak maxima are red-shifted to lower energies (1.49 eV and 1.29 eV respectively). This is due to the band gap narrowing that occurs when CdTe is alloyed with selenium [14], [36], [37]. The total CL signal in the CdTe region is small at 1.1 x10^6 counts, compared to 9.5 x10^6 counts over the same area in the Cd(Se,Te). In order to more directly compare the shapes and positions of the excitonic and DAP peaks for both materials, in Figure 4c we have superimposed the spectra such that both the DAP peaks are normalised and centred at a common photon energy. It can be seen from the figure that the energy difference between the DAP and excitonic peaks is larger in the Cd(Se,Te) than in the CdTe (0.2 eV vs 0.16 eV). Since the excitonic binding energy will be similar in materials with similar relative permittivity, this indicates that DAP emission in Cd(Se,Te) material is from deeper donor and acceptor states than in CdTe. This could either be because the deeper defects are not present in CdTe, or because they are present but not undergoing radiative recombination like they are in Cd(Se,Te). In addition, the normalised DAP peak is broader in the Cd(Se,Te) spectrum than in the CdTe, with a FWHM 43% larger. This again suggests that the addition of selenium to CdTe increases the density of donor and acceptor defects. Finally the CL spectra in Figure 4 show only a weak transition radiation signal [26] compared to luminescence generated by electron-hole pair recombination. In reference [26] transition radiation was found to dominate the TEM-CL signal in CdTe. The fact that this is not the case for our samples is due to the improved specimen preparation (i.e. less ion beam damage) from xenon FIB-milling (reference [26] on the other hand used conventional gallium ion beam milling). The suppression of transition radiation artefacts by xenon FIB is crucial for the correct interpretation of grain boundary contrast in this work.

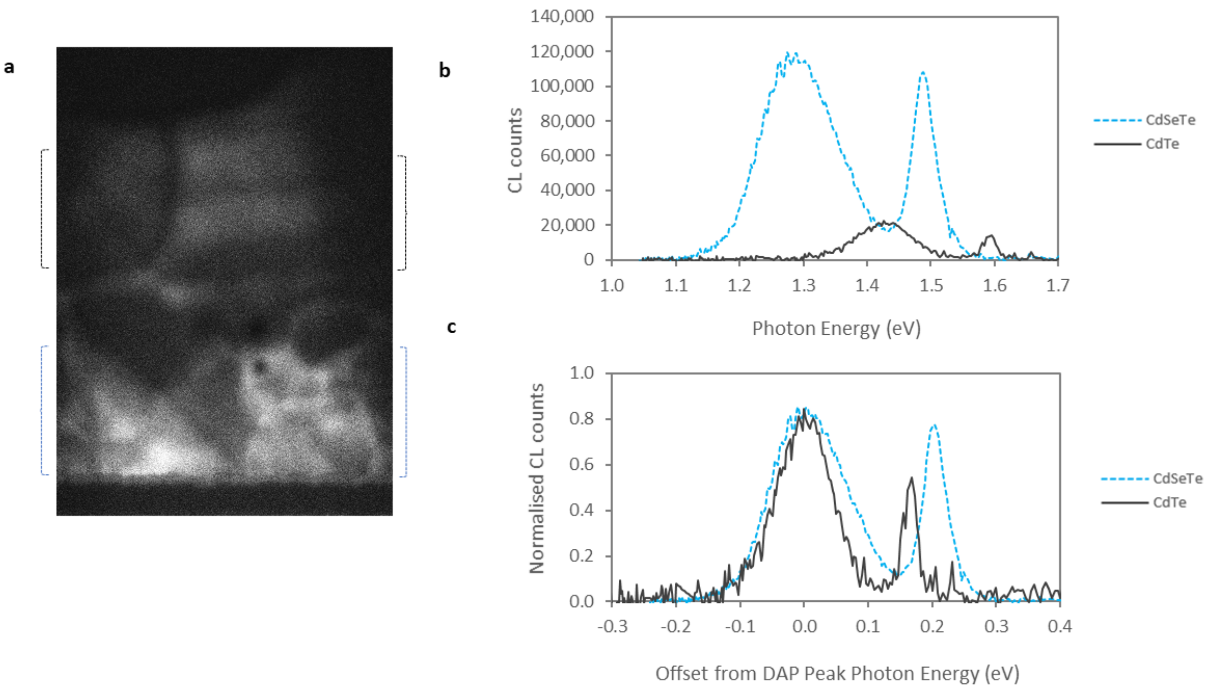

Figure 4. **a**, Low-temperature STEM-based CL map (-169.7 °C) of the panchromatic luminescence intensity over a cross-section of the treated Cd(Se,Te)/CdTe device, showing a brighter Cd(Se,Te) layer. **b**, Comparison of the average CL spectrum from the CdTe layer of the cross section (black curve, with the region shown by the top brackets in **a**) versus the spectrum from the Cd(Se,Te) layer (blue curve, with the region shown by the bottom brackets in **a**). **c**, normalised plot of the CdTe and Cd(Se,Te) spectra, with the DAP peaks centred on a common photon energy.

3. Discussion

The results presented here show that in $CdCl_2$ treated, selenium-graded CdTe cells there are significantly lower levels of non-radiative recombination at Cd(Se,Te) grain boundaries compared to CdTe boundaries. This suggests that selenium has a passivation effect on grain boundaries in Cd(Se,Te) material, in addition to what can already be achieved with chlorine passivation [6]. Given the high density and well-known detrimental effects of grain boundaries in thin-film polycrystalline solar cells this is an important finding. Alongside the grain interior passivation effect that has recently been discovered, the result provides an explanation for the superior carrier lifetimes and performance of selenium-alloyed CdTe. In addition, the results show that the more selenium that is present around the boundaries, the stronger the passivation effect at the boundary. This suggests that a selenium concentration above 10 at% at grain boundaries could have a stronger passivation effect than is already achieved and could lead to higher efficiency devices. It also suggests that if more selenium can be incorporated at grain boundaries at the back of the device, in the nominally CdTe region, then the amount of non-radiative carrier recombination in the absorber can be reduced and efficiencies increased (or, the CdTe layer could be removed entirely). This could be achieved by performing selenization treatments on the absorber to diffuse selenium into the grain boundaries.

In terms of the potential passivation mechanisms, it is not clear to what extent the reduced recombination is due to either: 1) the presence of selenium in the bulk material immediately either side of the grain boundaries, changing the electronic band structure that the boundary defects exist within; or 2) whether selenium interacts with the boundary defects themselves (i.e. selenium interacting directly with the wrong/dangling bonds); or a combination of the two. If there is no segregation of selenium at the Cd(Se,Te) grain boundaries (we could not detect any with TEM-EDX line scans) then it is worth noting that only ~1 in 10 of the atoms at the boundaries in our Cd(Se,Te) layer will be selenium, which corresponds to a density of 0.7-1.1 Se atoms per nm^2 on the boundary plane. This compares to a chlorine density of 0.8-2.0 atoms per nm^2 at $CdCl_2$ treated CdTe grain boundaries, which has been measured using SIMS [8].

4. Conclusion

In summary, in this work we have successfully performed TEM-based cathodoluminescence imaging on a selenium-graded CdTe solar cell by using xenon ion milling and sample cooling to significantly increase the luminescence signal from the TEM foil. The results show that selenium reduces harmful non-radiative recombination at grain boundaries in alloyed Cd(Se,Te) material, which helps to explain the superior carrier lifetimes and record performance of selenium graded CdTe solar cells. This could lead to further efficiency improvement of selenium-graded CdTe solar cells if concentrations at boundaries in the CdTe part of the absorber can be increased. In addition, the results demonstrate that TEM-CL has the potential to become a more standard technique for characterising solar cells, enabling a full package of microstructural, chemical and electronic characterisation at high resolution.

5. Experimental Section

Solar Cell Fabrication

The two cells used in this study were deposited on TEC10 glass substrates supplied by NSG Pilkington. The substrates comprise 3mm soda lime glass with a 400 nm fluorine doped SnO_2 transparent conducting oxide (TCO). Initially, a 100 nm MgZnO buffer layer (11% MgO, 89% ZnO) was deposited on the TCO by magnetron sputtering. This was followed by ~1.5 µm of Cd(Se,Te) deposited using Colorado State University's ARDS close space sublimation system [38]. During Cd(Se,Te) deposition a graphite source containing 40% CdSe was held at 575 °C, while the substrate was held at 420 °C. A ~3 µm layer of CdTe was then deposited with the CdTe source material held at 555 °C and the substrate at 500 °C (the CdTe and Cd(Se,Te) source material was supplied by 5N Plus). One of the cells then underwent a cadmium chloride activation process. During the process a $CdCl_2$ vapour was sublimated on to the back surface of the CdTe while the substrate was maintained at 430 °C for 600 seconds. It then went through a 110 s cooling step whilst held at 180 °C, removed from the vapour. Both devices then underwent a 110s copper doping treatment where copper chloride was deposited onto the back surface of the CdTe whilst held at 140 °C. The copper was then diffused into the device by a 220 °C, 220s anneal in vacuum. 30 nm of tellurium was then deposited onto the CdTe to form the back contact. The efficiency of the $CdCl_2$ treated device was measured at 16.8% (J_{SC} 26.8 mA/cm^2, V_{OC} 842 mV, Fill Factor 74.5%). The efficiency of the untreated device was measured at 0.01% (J_{SC} 0.1 mA/cm^2, V_{OC} 387 mV, Fill Factor 34.1%).

Transmission Electron Microscopy

The TEM lamellae for each sample were prepared by xenon ion milling in a FEI Helios Plasma-FIB using a standard in-situ lift out technique [12]. During final thinning the beam energy was 5 kV. STEM-CL was carried out in a JEOL 2100F FEG TEM at Brunel University. For the CL measurements the lamellae were cryogenically cooled to minus ~170 °C using liquid nitrogen. The microscope is fitted with a Gatan Vulcan CL system that has two parabolic mirrors, one either side of the TEM foil. A photomultiplier tube was used for acquiring the panchromatic CL images, and a CCD camera for the spectrum images. The electron beam energy during the CL measurements was 80kV. Due to the positioning of the parabolic mirrors of the CL holder, combined CL-EDX measurements were not possible, hence STEM-EDX imaging was performed separately. TEM and STEM-EDX measurements were carried out in a JOEL 2000FX TEM fitted with a Oxford Instruments EDX detector.

Acknowledgements

The authors at Loughborough University are grateful to the EPSRC CDT in New and Sustainable Photovoltaics for providing T.F. with a studentship, RCUK for providing funding through the EPSRC SUPERGEN SuperSolar Hub (EP/J017361/1), and the Loughborough Materials Characterisation Centre for access to the Helios PFIB, funded by the EPSRC grant EP/P030599/1. The authors at Colorado State University acknowledge support from NSF AIR, NSF I/UCRC and DOE SIPS programmes. The work at Colorado State University was supported by NSF award 1540007, NSF PFI:AIR-RA programme 1538733 and DOE SIPS award DE-EE0008177.

References

[1] M. Gloeckler, I. Sankin, and Z. Zhao, “CdTe Solar Cells at the Threshold to 20% Efficiency,” *IEEE J. Photovoltaics*, vol. 3, no. 4, pp. 1389–1393, Oct. 2013, doi: 10.1109/JPHOTOV.2013.2278661.

[2] C. Hagenorf, M. Ebert, M. Raugei, D. Lincot, J. Bengoechea, and M. Rodriguez, “Cener report number 30.2945.0-01: Assessment of performance, environmental, health and safety aspects of First Solar’s CdTe PV technology,” 2017. https://www.cener.com/wp-content/uploads/2017/03/30.2945.0-01-FirstSolar_EUReviewReport.pdf.

[3] M. A. Green, E. D. Dunlop, J. Hohl-Ebinger, M. Yoshita, N. Kopidakis, and A. W. Y. Ho-Baillie, “Solar cell efficiency tables (Version 55),” *Prog. Photovoltaics Res. Appl.*, vol. 28, no. 1, pp. 3–15, 2020, doi: 10.1002/pip.3228.

[4] R. Venkatasubramanian *et al.*, “18.2% (AM1.5) efficient GaAs solar cell on optical-grade polycrystalline Ge substrate,” in *Conference Record of the Twenty Fifth IEEE Photovoltaic Specialists Conference - 1996*, 1996, pp. 31–36, doi: 10.1109/PVSC.1996.563940.

[5] J. Benick *et al.*, “High-Efficiency n-Type HP mc Silicon Solar Cells,” *IEEE J. Photovoltaics*, vol. 7, no. 5, pp. 1171–1175, Sep. 2017, doi: 10.1109/JPHOTOV.2017.2714139.

[6] J. Moseley *et al.*, “Recombination by grain-boundary type in CdTe,” *J. Appl. Phys.*, vol. 118, 2015, doi: 10.1063/1.4926726.

[7] A. Abbas *et al.*, “The effect of cadmium chloride treatment on close-spaced sublimated cadmium telluride thin-film solar cells,” *IEEE J. Photovoltaics*, vol. 3, no. 4, pp. 1361–1366, 2013, doi: 10.1109/JPHOTOV.2013.2264995.

[8] D. Mao, C. E. Wickersham, and M. Gloeckler, “Measurement of chlorine

concentrations at CdTe grain boundaries," *IEEE J. Photovoltaics*, vol. 4, no. 6, pp. 1655–1658, 2014, doi: 10.1109/JPHOTOV.2014.2357258.

[9] J. D. Major, "Grain boundaries in CdTe thin film solar cells: a review," *Semicond. Sci. Technol.*, vol. 31, no. 9, p. 093001, 2016, doi: 10.1088/0268-1242/31/9/093001.

[10] C.-J. Tong and K. P. McKenna, "Passivating Grain Boundaries in Polycrystalline CdTe," *J. Phys. Chem. C*, vol. 123, no. 39, pp. 23882–23889, 2019, doi: 10.1021/acs.jpcc.9b08373.

[11] E. S. Barnard *et al.*, "3D Lifetime Tomography Reveals How CdCl2 Improves Recombination Throughout CdTe Solar Cells," *Adv. Mater.*, vol. 29, no. 3, 2017, doi: 10.1002/adma.201603801.

[12] Abbas, Ali (2014): The microstructure of thin film cadmium telluride photovoltaic materials. Loughborough University. Thesis. https://hdl.handle.net/2134/16389

[13] T. A. M. Fiducia *et al.*, "Large Area 3D Elemental Mapping of a MgZnO/CdTe Solar Cell with Correlative EBSD Measurements," in *WCPEC 2018 - A Joint Conference of 45th IEEE PVSC, 28th PVSEC and 34th EU PVSEC*, 2018, pp. 1702–1706, doi: 10.1109/PVSC.2018.8547876.

[14] T. A. M. Fiducia *et al.*, "Understanding the role of selenium in defect passivation for highly efficient selenium-alloyed cadmium telluride solar cells," *Nat. Energy*, vol. 4, no. 6, pp. 504–511, Jun. 2019, doi: 10.1038/s41560-019-0389-z.

[15] T. A. M. Fiducia *et al.*, "Defect Tolerance in as-deposited Selenium-alloyed Cadmium Telluride Solar Cells," in *2018 IEEE 7th World Conference on Photovoltaic Energy Conversion (WCPEC) (A Joint Conference of 45th IEEE PVSC, 28th PVSEC & 34th EU PVSEC),* Jun. 2018, pp. 0127–0130, doi: 10.1109/PVSC.2018.8547294.

[16] D. Kuciauskas, J. Moseley, P. Ščajev, and D. Albin, "Radiative Efficiency and Charge-Carrier Lifetimes and Diffusion Length in Polycrystalline CdSeTe Heterostructures," *Phys. Status Solidi - Rapid Res. Lett.*, vol. 1900606, pp. 1–6, 2019, doi: 10.1002/pssr.201900606.

[17] P. Ščajev *et al.*, "Excitation-dependent carrier lifetime and diffusion length in bulk CdTe determined by time-resolved optical pump-probe techniques," *J. Appl. Phys.*, vol. 123, no. 2, 2018, doi: 10.1063/1.5010780.

[18] J. Moseley *et al.*, "Cathodoluminescence analysis of grain boundaries and grain interiors in thin-film CdTe," *IEEE J. Photovoltaics*, vol. 4, no. 6, pp. 1671–1679, 2014, doi: 10.1109/JPHOTOV.2014.2359732.

[19] J. Guo *et al.*, "Effect of selenium and chlorine co-passivation in polycrystalline CdSeTe

devices," *Appl. Phys. Lett.*, vol. 115, no. 15, 2019, doi: 10.1063/1.5123169.

[20] J. Guo *et al.*, "Study of Effects of Cl and Se in CdSeTe Solar Cells Using Scanning Transmission Electron Microscopy," *Microsc. Microanal.*, vol. 25, no. S2, pp. 2150–2151, 2019, doi: 10.1017/s1431927619011486.

[21] R. Wang, M. Lan, and S. H. Wei, "Enhanced performance of Se-Alloyed CdTe solar cells: The role of Se-segregation on the grain boundaries," *J. Appl. Phys.*, vol. 129, no. 2, 2021, doi: 10.1063/5.0036701.

[22] A. Shah *et al.*, "Understanding the Copassivation Effect of Cl and Se for CdTe Grain Boundaries," *ACS Appl. Mater. Interfaces*, vol. 13, no. 29, pp. 35086–35096, Jul. 2021, doi: 10.1021/acsami.1c06587.

[23] X. Zheng *et al.*, "Recombination and bandgap engineering in CdSeTe/CdTe solar cells," *APL Mater.*, vol. 7, no. 7, p. 071112, 2019, doi: 10.1063/1.5098459.

[24] M. Amarasinghe, D. Albin, D. Kuciauskas, J. Moseley, C. L. Perkins, and W. K. Metzger, "Mechanisms for long carrier lifetime in Cd(Se)Te double heterostructures," *Appl. Phys. Lett.*, vol. 118, no. 21, p. 211102, 2021, doi: 10.1063/5.0047976.

[25] M. Kociak and L. F. Zagonel, "Cathodoluminescence in the scanning transmission electron microscope," *Ultramicroscopy*, vol. 176, pp. 112–131, 2017, doi: 10.1016/j.ultramic.2017.03.014.

[26] B. G. Mendis, A. Howkins, D. Stowe, J. D. Major, and K. Durose, "The role of transition radiation in cathodoluminescence imaging and spectroscopy of thin-foils," *Ultramicroscopy*, vol. 167, pp. 31–42, 2016, doi: 10.1016/j.ultramic.2016.05.002.

[27] X. Zheng, E. Colegrove, J. N. Duenow, J. Moseley, and W. K. Metzger, "Roles of bandgrading, lifetime, band alignment, and carrier concentration in high-efficiency CdSeTe solar cells," *J. Appl. Phys.*, vol. 128, no. 5, p. 053102, Aug. 2020, doi: 10.1063/5.0013726.

[28] A. H. Munshi *et al.*, "Effect of CdCl 2 passivation treatment on microstructure and performance of CdSeTe/CdTe thin-film photovoltaic devices," *Sol. Energy Mater. Sol. Cells*, vol. 186, no. May, pp. 259–265, 2018, doi: 10.1016/j.solmat.2018.06.016.

[29] T. Bidaud, J. Moseley, M. Al-jassim, M. Amarasinghe, and W. K. Metzger, "Spatially and spectrally resolved defects in polycrystalline CdTe thin films revealed by quantitative cathodoluminescence," 2019 IEEE 46th Photovoltaic Specialists Conference (PVSC), 2019, pp. 1-4, doi: 10.1109/PVSC40753.2019.9198976.

[30] J. Moseley *et al.*, "Luminescence methodology to determine grain-boundary, grain-interior, and surface recombination in thin-film solar cells," *J. Appl. Phys.*, vol. 124,

no. 11, 2018, doi: 10.1063/1.5042532.

[31] T. A. M. Fiducia *et al.*, “Three-Dimensional Imaging of Selenium and Chlorine Distributions in Highly Efficient Selenium-Graded Cadmium Telluride Solar Cells,” *IEEE J. Photovoltaics*, vol. PP, pp. 1–5, 2019, doi: 10.1109/JPHOTOV.2019.2955313.

[32] B. G. Mendis, L. Bowen, and Q. Z. Jiang, “A contactless method for measuring the recombination velocity of an individual grain boundary in thin-film photovoltaics,” *Appl. Phys. Lett.*, vol. 97, no. 9, pp. 0–3, 2010, doi: 10.1063/1.3486482.

[33] Y. Yoon *et al.*, “Unveiling Defect-Mediated Charge-Carrier Recombination at the Nanometer Scale in Polycrystalline Solar Cells,” *ACS Appl. Mater. Interfaces*, vol. 11, no. 50, pp. 47037–47046, 2019, doi: 10.1021/acsami.9b14730.

[34] B. Bissig *et al.*, “On a better estimate of the charge collection function in CdTe solar cells: Al2O3 enhanced electron beam induced current measurements,” *Thin Solid Films*, vol. 633. pp. 218–221, 2017, doi: 10.1016/j.tsf.2016.08.012.

[35] V. Consonni, G. Feuillet, and S. Renet, “Spectroscopic analysis of defects in chlorine doped polycrystalline CdTe,” *J. Appl. Phys.*, vol. 99, no. 5, 2006, doi: 10.1063/1.2174117.

[36] D. E. Swanson, J. R. Sites, and W. S. Sampath, “Co-sublimation of CdSe x Te 1 À x layers for CdTe solar cells,” *Sol. Energy Mater. Sol. Cells*, vol. 159, pp. 389–394, 2017, doi: 10.1016/j.solmat.2016.09.025.

[37] M. J. Watts, T. A. M. Fiducia, B. Sanyal, R. Smith, J. M. Walls, and P. Goddard, “Enhancement of photovoltaic efficiency in CdSe x Te 1− x (where 0 ⩽ x ⩽ 1): insights from density functional theory,” *J. Phys. Condens. Matter*, vol. 32, no. 12, p. 125702, Mar. 2020, doi: 10.1088/1361-648X/ab5bba.

[38] D. E. Swanson *et al.*, “Single vacuum chamber with multiple close space sublimation sources to fabricate CdTe solar cells,” *J. Vac. Sci. Technol. A Vacuum, Surfaces, Film.*, vol. 34, no. 2, p. 021202, 2016, doi: 10.1116/1.4941071.

Supporting Information

Passivation of Grain Boundaries in Selenium-alloyed CdTe Solar Cells

Thomas Fiducia, Ashley Howkins, Ali Abbas, Budhika Mendis, Amit Munshi, Kurt Barth, Walajabad Sampath, and John Walls

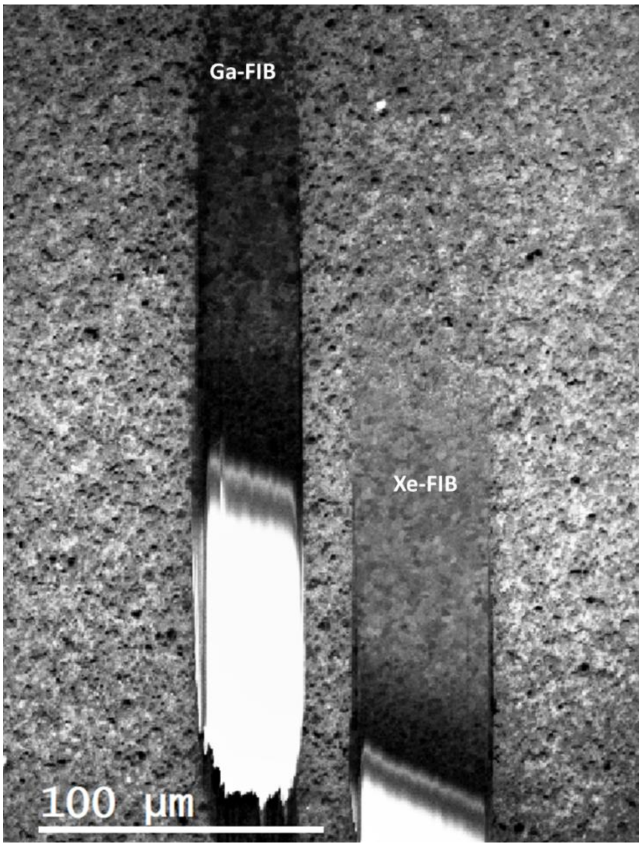

Supplementary Figure 1. SEM-based CL map of the luminescence intensity from Ga-milled and Xe-milled bevels in the treated Cd(Se,Te)/CdTe bilayer device (ion beam milling was performed at 30 kV for both trenches and at an angle of 7º to the substrate).

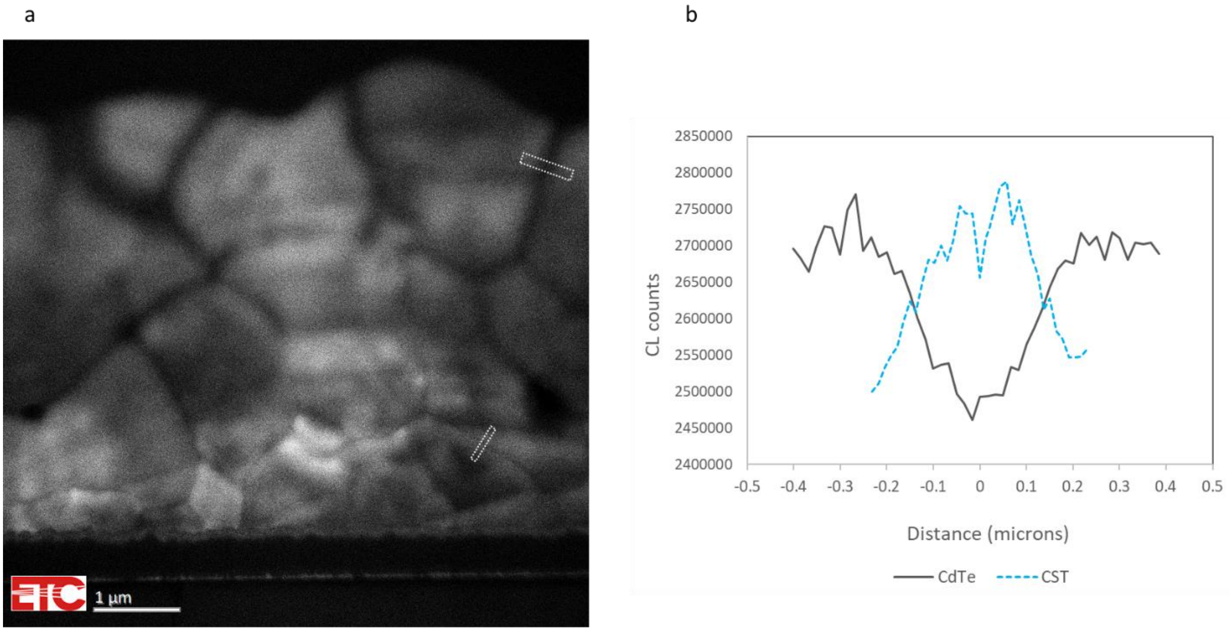

Supplementary Figure 2. **a**, STEM-based cathodoluminescence (CL) map of the panchromatic CL intensity over the cadmium chloride treated Cd(Se,Te)/CdTe bilayer cross-section, as seen in Figure 2d in the main text. Boxes show the positions where the line profiles in **b** are taken. **b**, Line profiles of the CL signal across grain boundaries CdTe (black) and Cd(Se,Te) (blue) layers. In each case the grain boundary position is arbitrarily set to zero µm.

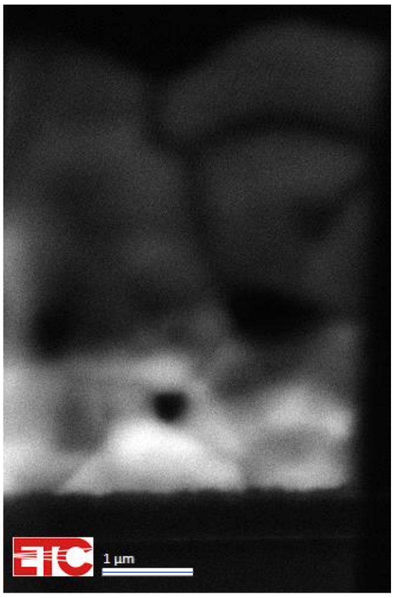

Supplementary Figure 3. STEM-based CL map of the panchromatic luminescence intensity over a cross-section of the treated Cd(Se,Te)/CdTe device, showing brighter Cl intensity and thin grain boundary contrast in the Cd(Se,Te) layer.

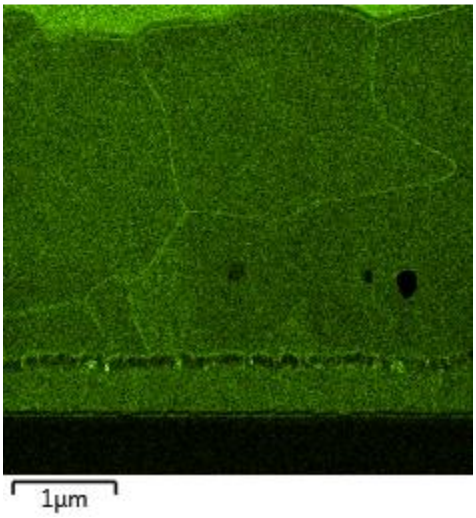

Supplementary Figure 4. TEM-EDX map of the chlorine distribution in the $CdCl_2$ treated cell, from a different region as that shown in Figure 2 in the main text.